UCSF
UC San Francisco Previously Published Works

Title

Synthetic Knee MRI T1p Maps as an Avenue for Clinical Translation of Quantitative Osteoarthritis Biomarkers.

Permalink

https://escholarship.org/uc/item/9p91t229

Journal

Bioengineering, 11(1)

ISSN

2306-5354

Authors

Tong, Michelle

Tolpadi, Aniket

Bhattacharjee, Rupsa

et al.

Publication Date

2023-12-24

DOI

10.3390/bioengineering11010017

Peer reviewed

Article

Synthetic Knee MRI $T_{1\rho}$ Maps as an Avenue for Clinical Translation of Quantitative Osteoarthritis Biomarkers

Michelle W. Tong [1,2,*], **Aniket A. Tolpadi** [1,2], **Rupsa Bhattacharjee** [1], **Misung Han** [1], **Sharmila Majumdar** [1] **and Valentina Pedoia** [1]

[1] Department of Radiology and Biomedical Imaging, University of California San Francisco, San Francisco, CA 94143, USA; sharmila.majumdar@ucsf.edu (S.M.); valentina.pedoia@ucsf.edu (V.P.)
[2] Department of Bioengineering, University of California Berkeley, Berkeley, CA 94720, USA
[*] Correspondence: michelle.tong2@ucsf.edu

Abstract: A 2D U-Net was trained to generate synthetic $T_{1\rho}$ maps from T_2 maps for knee MRI to explore the feasibility of domain adaptation for enriching existing datasets and enabling rapid, reliable image reconstruction. The network was developed using 509 healthy contralateral and injured ipsilateral knee images from patients with ACL injuries and reconstruction surgeries acquired across three institutions. Network generalizability was evaluated on 343 knees acquired in a clinical setting and 46 knees from simultaneous bilateral acquisition in a research setting. The deep neural network synthesized high-fidelity reconstructions of $T_{1\rho}$ maps, preserving textures and local $T_{1\rho}$ elevation patterns in cartilage with a normalized mean square error of 2.4% and Pearson's correlation coefficient of 0.93. Analysis of reconstructed $T_{1\rho}$ maps within cartilage compartments revealed minimal bias (-0.10 ms), tight limits of agreement, and quantification error (5.7%) below the threshold for clinically significant change (6.42%) associated with osteoarthritis. In an out-of-distribution external test set, synthetic maps preserved $T_{1\rho}$ textures, but exhibited increased bias and wider limits of agreement. This study demonstrates the capability of image synthesis to reduce acquisition time, derive meaningful information from existing datasets, and suggest a pathway for standardizing $T_{1\rho}$ as a quantitative biomarker for osteoarthritis.

Keywords: $T_{1\rho}$ map; T_2 map; knee; MRI; osteoarthritis; synthesis; generative AI; deep learning; CNN; U-Net

1. Introduction

Knee osteoarthritis (OA) is a leading cause of chronic disability and pain worldwide, impacting 23% of individuals over age 40 and reducing mobility for 80% of those diagnosed [1,2]. This irreversible condition is characterized by the degeneration of articular cartilage which significantly impacts quality of life and thus necessitates early detection. As individuals age and OA progresses, the structural integrity of the cartilage extracellular matrix declines, resulting in a reduced ability to retain water, proteoglycan disorganization, and cartilage degeneration [3,4]. Several risk factors that contribute to OA include age, weight (obesity), sex (female), prior knee injury, participation in high-impact sports, and occupations that involve heavy physical labor [5–7]. Intervention efforts aim to reduce OA progression through non-invasive and non-pharmacological interventions such as self-management, exercise, and weight loss. In cases of advanced OA, treatment strategies include non-steroid anti-inflammatory pain medication, intra-articular injections, and surgeries such as total knee arthroplasty [8–10].

Standard clinical diagnosis of OA involves evaluation of the patient's age, self-reported symptoms, and morphological changes such as radiographic identification of osteophytes and joint-space narrowing [11,12]. However, these criteria are more characteristic of advanced disease once considerable damage has occurred and often require more invasive

treatment strategies [12,13]. Furthermore, radiographic changes are poor predictors of cartilage loss [14] and have weak associations with symptoms [15,16]. MRI enables visualization of soft tissue in joint structures without radiation and achieves higher sensitivity to pathological changes indicative of OA [17,18]. However, the characterization of cartilage injury from structural MRI varies, leading to accurate assessments, instances of underestimation, and instances of overestimation across pathology and cartilage compartments [19–21].

Unlike radiography and structural MRI, compositional non-contrast MRI techniques such as $T_{1\rho}$ and T_2 mapping are sensitive to early biochemical changes in cartilage that precede morphological changes in OA [22–25]. T_2 relaxation measures free water (65–80% cartilage total weight [3]) proton movement, and thus elevated values may indicate collagen/extracellular matrix degeneration [26]. $T_{1\rho}$ relaxation describes spin-lattice relaxation in the rotating frame which captures changes between water protons and their macromolecular environment, mainly proteoglycans (10–15% cartilage wet weight [3]). Increases in $T_{1\rho}$ values are associated with proteoglycan degeneration which is characteristic of OA, offering greater sensitivity to OA onset than T_2 values. Additionally, $T_{1\rho}$ values reflect patient-reported pain, symptoms, and loss of function (KOOS) [25,27,28].

$T_{1\rho}$ mapping shows promise for early OA detection with slightly greater sensitivity than T_2 [29], yet further validation of both sequences is required to increase confidence in $T_{1\rho}$ maps as viable quantitative imaging biomarkers for clinical practice [30–32]. However, the addition of $T_{1\rho}$ mapping to standard imaging protocols faces challenges, including prolonged image acquisition times, image processing requirements, and often SAR concerns that have prevented its widespread adoption in the clinic [33–35]. In contrast, T_2 mapping has gained broader adoption for clinical and research purposes, often being acquired in the absence of $T_{1\rho}$ mapping, as seen in large studies like the Osteoarthritis Initiative [36].

Image synthesis via deep learning has been gaining popularity in aiding clinical workflows by overcoming limitations with acquisition time, labor, and expenses [37,38]. In previous knee MRI synthesis studies, deep learning models were developed to generate images with new contrast [39], augment datasets by generating images with the same contrast [40], and standardize MR images to reduce scanner effects prior to downstream processing [41]. While newer architectures have emerged [42], convolutional neural networks (CNNs) remain valuable as a data-driven approach to learning image feature representations tailored to perform specific tasks well [43–46]. This study aims to generate synthetic $T_{1\rho}$ maps from T_2 maps to derive new information that can improve clinical outcomes and create possibilities for further analysis of large cohort studies.

This work makes the following contributions.

- This study proposes medical image synthesis as a repeatable and efficient method for extracting quantitative biomarkers. This methodology may overcome limitations in hardware acquisition speed, variations across scanner sites, and availability of quantitative imaging sequences in existing datasets or at scanner locations.
- To the best of the authors' knowledge, this is the first study to synthesize $T_{1\rho}$ maps from T_2 maps for knee MRI scans. This contribution is valuable for characterizing and assessing $T_{1\rho}$ as a biomarker for knee OA, as it reduces acquisition time and facilitates the extraction of meaningful information.
- While there is a substantial body of research on U-Nets for image segmentation, the utility of CNNs for image synthesis and clinical deployment is less known [45,46]. This study develops an image synthesis algorithm using well-studied network architecture and performs comprehensive evaluation across four diverse cohorts.
- This study provides clarity on the network's ability to perform synthesis (1) within a well-constrained held-out test dataset and (2) in a new context where images were acquired under varied imaging conditions. These findings provide a greater understanding of the strengths and limitations of model architecture and the feasibility of clinical translation.

2. Materials and Methods

2.1. Cohort Description

After obtaining IRB approval for this retrospective study, 897 knee MRI scans were identified from four cohorts, spanning 594 healthy and diseased patients. For network development, 509 unilateral knees were used from two cohorts: (A) a UCSF study on ACL injury [47] and (B) a multi-center study conducted at UCSF (San Francisco, CA, USA), Mayo Clinic (Rochester, MN, USA), and Hospital for Special Surgery (New York, NY, USA) on recovery from ACL tears and reconstructive surgery [35,48]. Scans were acquired before, 6 months after, and 12 months after injury. Out-of-distribution performance was evaluated on external data from two cohorts: (C) 343 unilateral knee scans in a clinical setting and (D) bilateral knee scans acquired simultaneously from 23 subjects without ACL tear or reconstruction but with idiopathic OA at the knee or the hip. A description of the dataset is summarized in Table 1.

Table 1. Cohort demographics and scan equipment breakdown for 897 knees in this study. Age and BMI (mean $\pm$ stdev.) are known covariates of OA indication from relaxation times.

Cohort	A	B	C	D
Study				
Institution	UCSF	UCSF, HSS, Mayo	UCSF	UCSF
Acquisition setting	Research	Research	Clinical	Research
Demographics				
Number of knees	273	235	343	46
Number of patients	75	175	321	23
Age	30 ± 8	29 ± 14	37 ± 13	58 ± 13
Males/Females	10:7	10:8	7:5	10:9
BMI	72.9 ± 13.1	74.3 ± 12.1	77.3 ± 15.9	74.2 ± 16.1
Scanners and Coil Combination Method				
GE Signa MR750 (GE Healthcare, Waukesha, WI, USA), sum-of-square coil combination	$n = 56$	$n = 155$	$n = 343$	---
GE Signa MR750W (GE Healthcare, Waukesha, WI), sum-of-square coil combination	$n = 216$	$n = 67$	---	---
GE Signa PET-MRI (GE Healthcare, Waukesha, WI), sum-of-square coil combination	---	$n = 13$	---	---
GE Signa Premier (GE Healthcare, Waukesha, WI), adaptive coil combination	---	---	---	$n = 46$
Knee Coil				
8-channel transmit/receive knee coil array (In-Vivo Corp., Gainesville, FL, USA)	$n = 273$	$n = 235$	$n = 278$	---
16-channel medium GEM flex-coil array (Neo-Coil, Pewaukee, WI, USA)	---	---	$n = 32$	$n = 46$ (2 simultaneous acquisitions)
16-channel large GEM flex-coil array (Neo-Coil, Pewaukee, WI)	---	---	$n = 25$	---
8-channel cardiac coil array (GE Healthcare, Waukesha, WI)	---	---	$n = 8$	---

2.2. Image Acquisition and Processing

Scanner and coil array information for each cohort is specified in Table 1. All the scans were acquired at 3 Tesla. The network was trained with cohorts A and B, whose data was collected on three different scanners using a single type of knee coil. For cohort C, images were acquired as an add-on to the standard clinical procedure on one scanner using four different coils. For cohort D, images were acquired on a different scanner using two coil arrays simultaneously for bilateral knee image acquisition.

T_{1p}/T_2-weighted images were acquired from magnetization-prepared angle-modulated partitioned k-space spoiled gradient echo snapshots (MAPSS) in the sagittal plane [49]. For unilateral knee MRI (cohorts A–C), T_{1p} weighted MAPSS with fat suppression was performed at a spin-lock frequency of 500 Hz, and a spin lock time (TSL) over 0/2/4/8/12/20/40/80 or 0/10/40/80 ms. T_2-weighted MAPSS was acquired at T2-preparation time (TE) of 0/12.9/25.7/51.4 ms or 2.9/13.6/24.3/45.6 ms. Other imaging parameters included time between magnetization preparations as TR = 1.2 s; FOV = 14 cm; slice thickness = 4 mm; acquisition matrix = 256 × 128; reconstructed matrix = 256 × 256; readout bandwidth = ±62.5 kHz; 5–10 ms TR (per view); 64 views per preparation; number of slices = 24; ky acceleration = 2). MAPSS was also used to acquire echo images for the bilateral knee scans (cohort D) with adjusted parameters: TSL = 0/10/40/80 ms only; TE = 0/12.9/25.7/51.4 ms only; increased slice number of 88; TR = 5.1 ms; 76 views per preparations; ky and kz accelerations of 2 × 3.

T_2 and T_{1p} maps were calculated as follows: all relevant echo images were registered to the TE/TSL = 0 ms shared echo using 3D affine registration with a normalized mutual information criterion [50]. Prior to T_{1p} and T_2 map generation, the bilateral scans were automatically divided into left and right unilateral scans. Levenberg–Marquardt mono-exponential fitting of registered echoes yielded ground truth T_{1p} and T_2 maps [51].

2.3. Segmentation

Cartilage segmentations were obtained from the first echo (TE/TSL = 0 ms) using a 3D V-Net architecture trained on data from research studies. To achieve further granular analysis of cartilage compartments, an automatic segmentation algorithm [52] used the first echo (TE/TSL = 0 ms) images to identify cartilage compartment regions for the medial femoral condyle (MF), lateral femoral condyle (LF), medial tibial (MT), lateral tibial (LT), patellar (PAT), and trochlea (TRO) cartilage.

2.4. Training

Input T_2 map slices from cohorts A and B were split into training, validation, and testing using a 65%:15%:20% split such that each subject was only in one subset and each study was similarly represented. T_{1p} map slices were predicted from T_2 map slices using a 2D U-Net network (Figure 1) with 8 convolutional layers, ReLU activation, batch normalization, and skip connections. The network encodes T_2 maps in a low-resolution high-dimensional space before upsampling the latent feature representations to predict T_{1p} maps. Network weights were optimized until validation loss stopped decreasing and 4-fold cross-validation was performed. A hyperparameter search identified the optimal loss function, input intensity scaling, and learning rate to minimize the normalized root mean squared error between the predicted and ground truth maps.
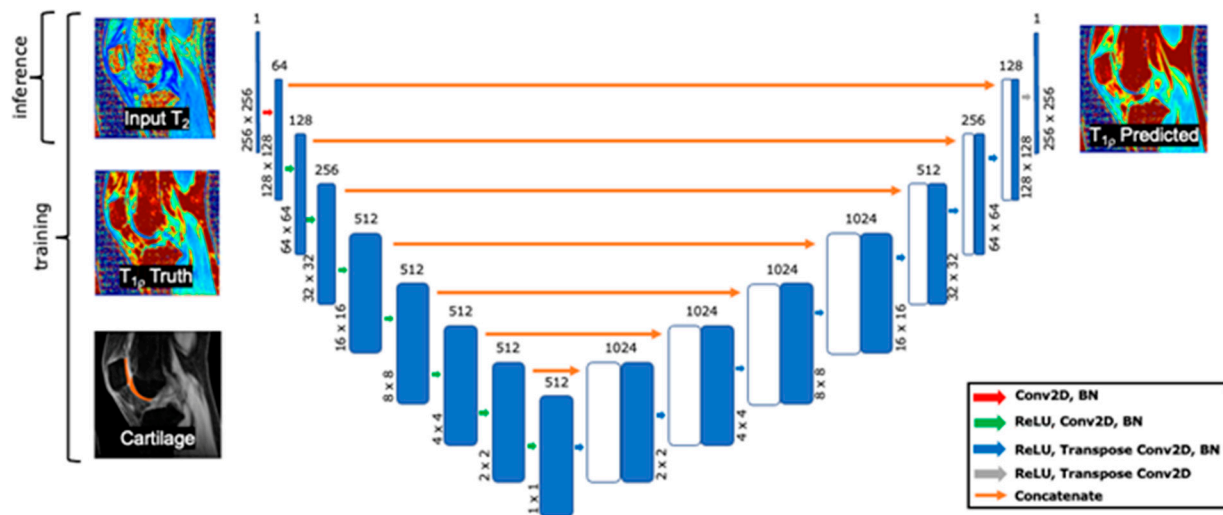
Figure 1. Synthetic $T_{1\rho}$ maps were generated from T_2 maps using this U-Net network. The optimal network that minimized the cartilage NMSE used combination of L1 and L2 loss in the cartilage and surrounding area.

2.5. Within-Distribution Testing and Performance Evaluation for Image Generation

For model evaluation, the test dataset comprised 101 knees from 57 patients (cohorts A and B). Performance was evaluated across voxels in the entire imaging volume and within cartilage compartments using the NMSE, structural similarity (SSIM), peak signal-to-noise ratio (PSNR), Pearson's correlation coefficient (CORR), and visual inspection. All models were implemented in Pytorch (Python 3.7; Pytorch 1.9.1, 1 GPU, 24 or 12 GB RAM).

The optimal network was selected based on the lowest NMSE in the cartilage segmentation and used a weighted loss function with L2 loss for the cartilage region and L1 loss for the remainder of the image Equation (1). Input T_2 maps were clipped to values between 0 and 150 to reduce the effect of background noise.

$$\text{loss} = 1.5 \times \text{L2\_loss}\left(y_{\text{cartilage}}, \hat{y}_{\text{cartilage}}\right) + \text{L1\_loss}\left(y_{\text{background}}, \hat{y}_{\text{background}}\right). \quad (1)$$

2.6. Out-of-Distribution Inference Testing for Model Generalizability

To evaluate model generalizability, inference was performed on data that differed from the training data. Whereas the model was trained on data collected using a single knee coil in a research environment (cohort A and B), synthetic $T_{1\rho}$ maps were generated for data collected using various knee coils in a clinical setting (cohort C) and using two knee coils simultaneously in a research setting (cohort D) (Table 1).

2.7. Statistical Analysis: Quantitative Correlation

For both in-distribution and external cohort testing, Pearson's correlation coefficients were calculated between the average synthesized and ground truth $T_{1\rho}$ values in each cartilage compartment to assess the quality of synthesis [53]. Reported values include Pearson's r to provide insight into the strength and direction of the relationship, the degrees of freedom that specify the dimensionality in which variance is estimated, and the two-tailed *p*-value to determine statistical significance ($p < 0.001$). Bland–Altman plots were generated for the average $T_{1\rho}$ value in the cartilage compartments to demonstrate the spread as well as the limits of agreement [54,55]. The statistical testing was performed using Python (version 3.7).

3. Results

3.1. In-Distribution Cohort Test Set

3.1.1. Example Demonstration

T_2 input maps, ground truth $T_{1\rho}$ maps, and predicted $T_{1\rho}$ maps for four patients are shown in Figure 2. (a,c) Patients shown from a study at UCSF and HSS presented elevated $T_{1\rho}$ values in the anterior and posterior cartilage relative to the central cartilage. (b,d) Patients shown from the multi-center study at UCSF and Mayo exhibited textural changes between the T_2 and $T_{1\rho}$ values in the patellar and trochlear cartilage. In all cases, the synthetic $T_{1\rho}$ images maintained excellent reconstructions that captured the elevation patterns in ground truth images.
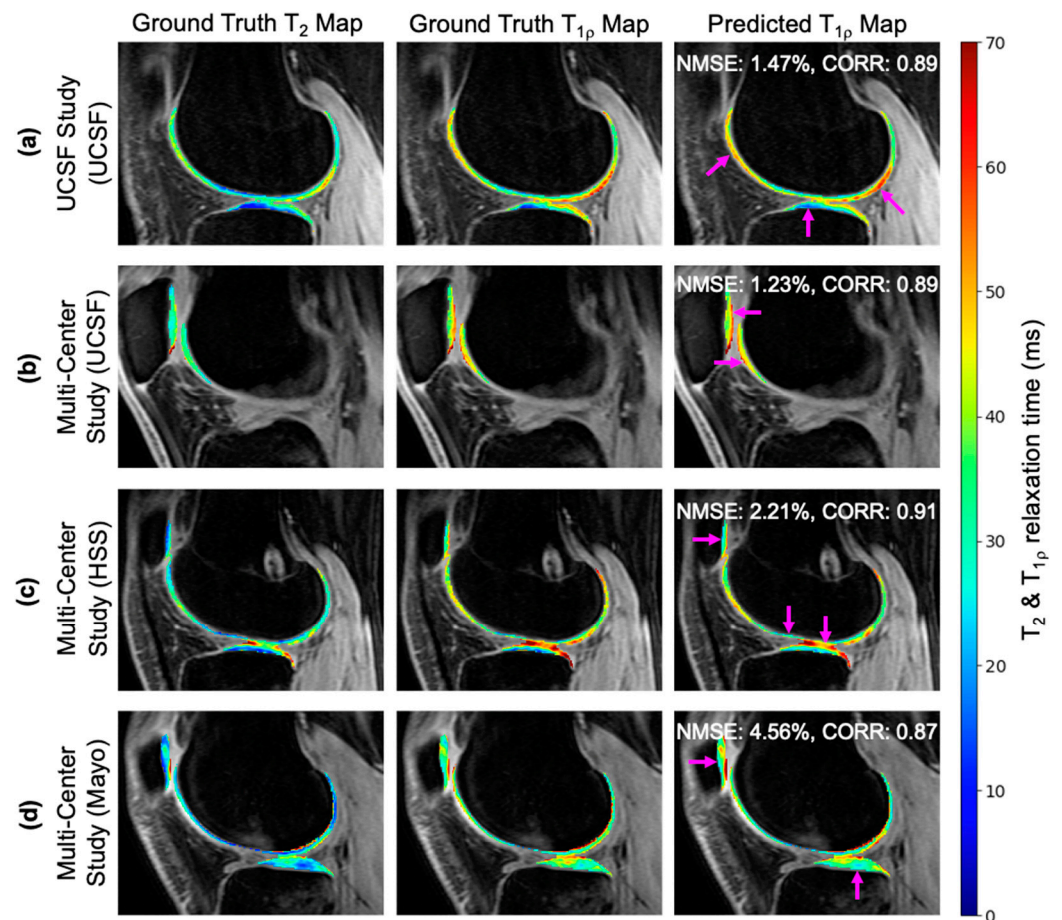

Figure 2. Four knees from patients who participated in one of two studies: (**a**) the UCSF (cohort A) study or (**b**–**d**) the multi-center (cohort B) study at one of three centers. Input ground truth T_2 maps exhibit distinct intensity elevation and textural patterns compared to ground truth $T_{1\rho}$ maps. Nevertheless, predicted $T_{1\rho}$ maps generated by the CNN preserve these differences, as indicated by the regions marked by the arrows.

3.1.2. Image Generation Performance Evaluation

Table 2 provides a summary of the NMSE, SSIM, PSNR, and CORR values across the entire test set and by cohort. The metrics are reported for the cartilage region and the entire imaging volume which includes muscle, bone, and background in addition to knee cartilage. Across all studies, the network performed well with low NMSE (2.41 ± 1.51%, range 2.18–2.61%) and strong correlation in the cartilage segmentation. Similarity metrics within each cartilage compartment (Table A1) found the PSNR of the UCSF study was 5.0 ± 2.0 higher than the multi-center study, with similar CORR values ranging from 0.81 to 0.9, and similar NMSEs ranging from 2.04% to 4.78% for all compartments except patellar cartilage from the multi-center study, which had a NMSE of 5.79%.

Table 2. Similarity metrics between ground truth and predicted T_{1p} maps for patients who participated in the UCSF study, multi-center study, and across both studies.

Similarity Metric	NMSE (%)		PSNR	CORR	SSIM
avg ± stdev. across patients	*volume*	*cartilage*	*cartilage*	*cartilage*	*volume*
All Studies	4.18 ± 1.97	2.41 ± 1.51	23.99 ± 1.98	0.87 ± 0.08	0.62 ± 0.06
UCSF Study	4.84 ± 2.42	2.61 ± 1.47	24.00 ± 1.78	0.85 ± 0.07	0.62 ± 0.06
Multi-center Study	3.42 ± 0.67	2.18 ± 1.53	23.97 ± 2.17	0.88 ± 0.08	0.62 ± 0.05

3.1.3. Quantitative Correlation Analysis

Bland–Altman plots of held-out test data in Figure 3 reveal minimal bias and tight limits of agreement across the entire cartilage region. Across each of the six cartilage compartments, bias remained minimal and limits of agreement were slightly wider than the entire cartilage region analysis. This discrepancy is likely attributed to fewer voxels in the compartment average. Data from the two in-distribution studies (cohorts A and B) have different ranges of ground truth T_{1p} values, with the mean T_{1p} for the multi-center study being 5.48 ms higher. Despite this difference, similar limits of agreement and biases indicate the network is robust to various values. The absence of underestimated low T_{1p} values suggests the network has learned a lower bound of relevant T_{1p} values, while higher T_{1p} values are well represented on both sides of the line of equality. Further examination of the cartilage compartments found the patellar and trochlear cartilage had wider limits of agreement than the other compartments. Within a study, mean T_{1p} values were similarly represented across all the cartilage compartments (Figure A1). Correlation plots show exceptional agreement across studies in all cartilage regions (Pearson's r = 0.93) and cartilage compartments (Pearson's r = 0.99) (Figure 4).
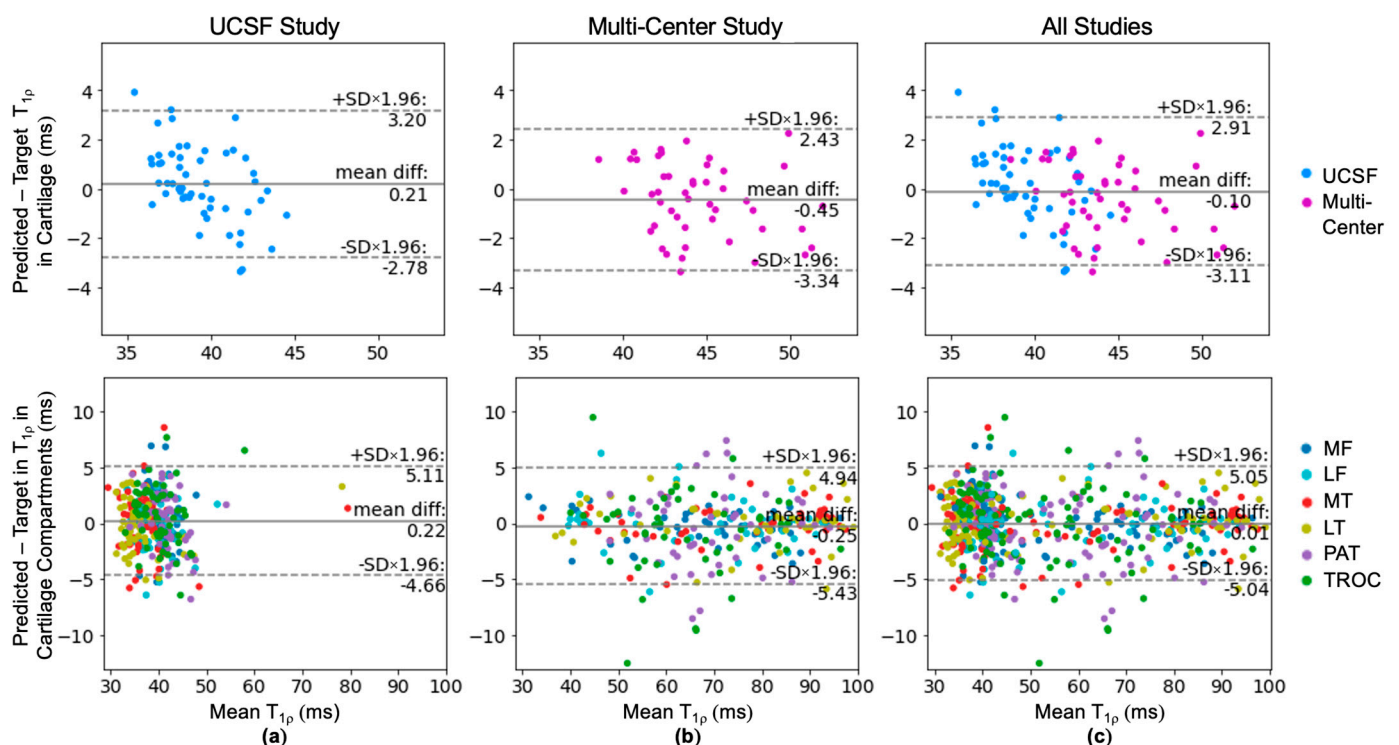

Figure 3. Bland-Altman plots for predicted T_{1p} performance across the entire cartilage tissue and within 6 cartilage compartments for (**a**) the UCSF study (cohort A), (**b**) the multi-center study (cohort B), and (**c**) all in-distribution studies (cohorts A and B). Model performance in each study reveals slight biases that were relatively consistent between the entire cartilage region and cartilage compartments. Across all studies, the network performed excellent synthesis with minimal bias and tight limits of agreement within a range that is clinically significant for cartilage region analysis.
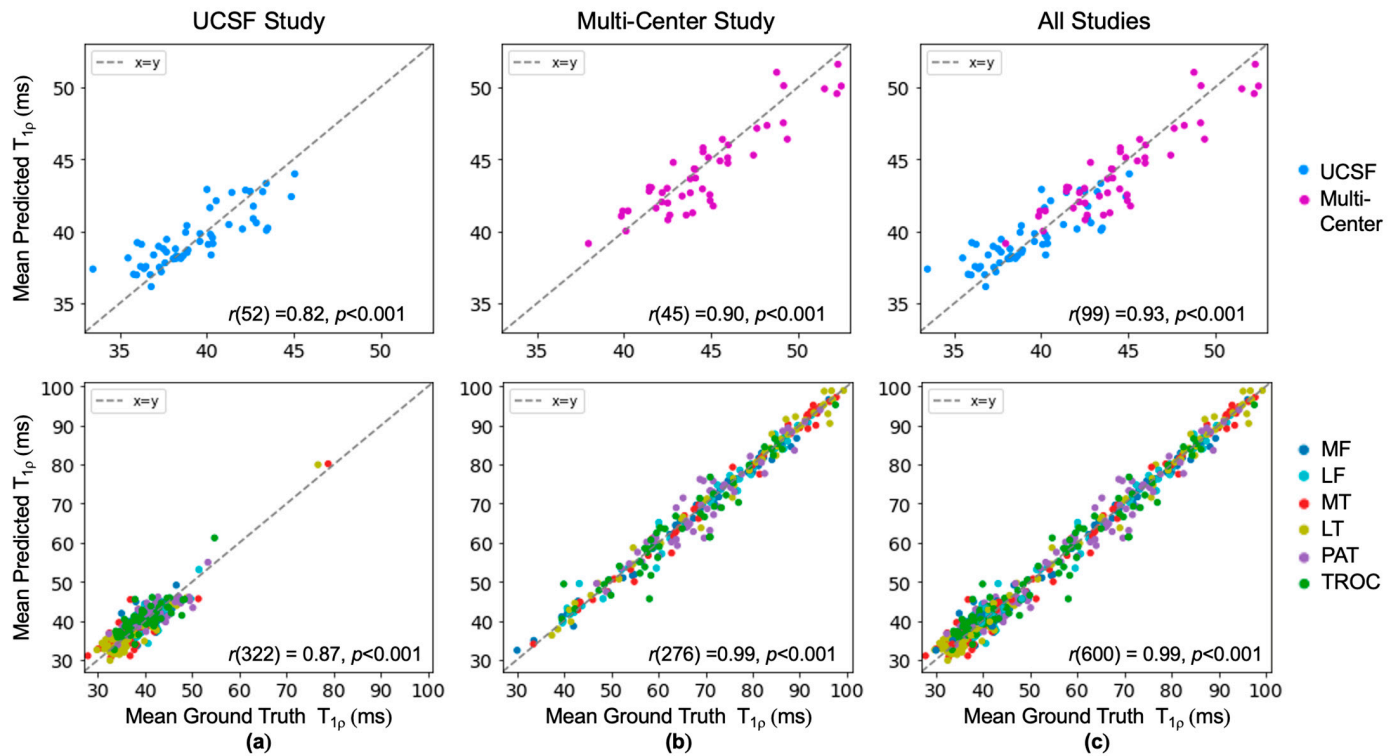
Figure 4. Ground truth T_{1p} and predicted T_{1p} values in knee cartilage were strongly correlated indicated by statistically significant Pearson's r values for (**a**) the UCSF study (cohort A), (**b**) the multi-center study (cohort B), and (**c**) all in-distribution studies (cohorts A and B). Mean predicted T_{1p} values were close to the dashed unity line.

3.2. External Cohort Inference Set

3.2.1. Example Demonstration

Synthesis of new information was assessed in T_{1p} maps of four knees: two from the clinical dataset and two from the bilateral knee study (Figure 5). (a) For a clinical knee acquired using a knee T/R coil, the network used T_2 maps to infer the appropriate intensity gradient of T_{1p} in the anterior horn and posterior horn relative to the central femoral cartilage. (b) For a clinical knee acquired with a flex coil, patterns were generally well maintained but the extent of T_{1p} elevation in the anterior femoral cartilage was not fully realized. (c,d) For bilateral study knees acquired with two flex coil arrays, T_{1p} map intensities are well synthesized, which is demonstrated (c) in the tibia and patellar relative to the central femoral cartilage, and (d) in the posterior femoral cartilage relative to the central cartilage. These four example cases have cartilage slice NMSE ranging from 5.85 to 7.64%, which was higher than the development dataset; yet, in all cases, the relative intensity patterns were still preserved.

3.2.2. Image Generation Performance Evaluation

Similarity metrics reported in Table 3 exhibited a slight decrease in performance for out-of-distribution datasets (cohorts C and D) compared to held-out test data from the development dataset (cohorts A and B). For the entire clinical dataset acquired with a unilateral knee coil, performance metrics were better than the bilateral dataset. NMSE in cartilage tissue increased by 2.02% in comparison to the development dataset, and performance metrics were best for data collected with the same coil as the training dataset. For the bilateral dataset, NMSE in cartilage tissue increased by 4.85% compared to the development dataset. Consistent with trends in the development cohort, cartilage NMSE is lower than the NMSE across the entire knee volume.
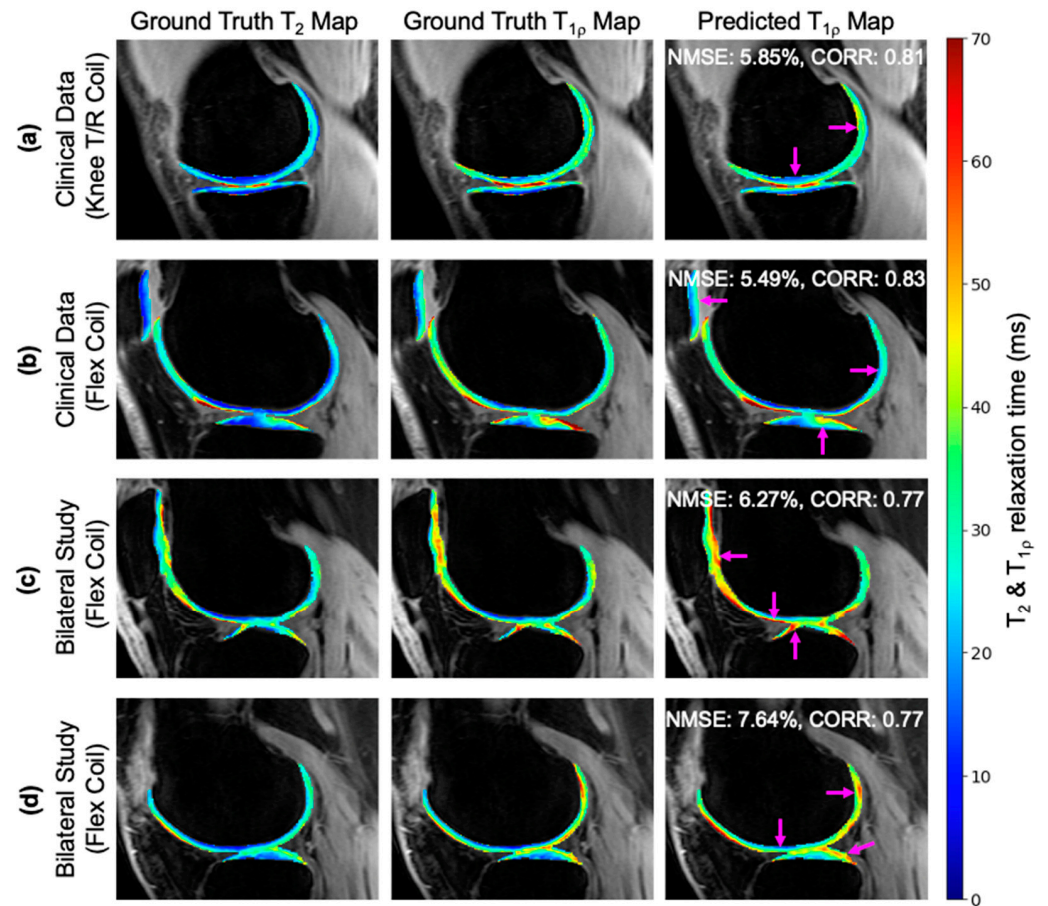
Figure 5. (**a**–**d**) Model inference was performed on data outside of the training data distribution to generate synthetic $T_{1\rho}$ maps. Images are shown for 4 knees collected in (**a**,**b**) a clinical setting or (**c**,**d**) as part of a bilateral acquisition research study. Input ground truth T_2 maps, ground truth $T_{1\rho}$ maps, and predicted $T_{1\rho}$ maps demonstrate the network effectively retained the elevation and textural patterns even though NMSE was higher than the development dataset. Regions marked by arrows showcase the network's ability to synthesize $T_{1\rho}$ maps despite varied relative differences in T_2 map elevation.

Table 3. Synthetic $T_{1\rho}$ maps were generated for out-of-distribution data to test model generalizability. Performance was assessed per knee coil used during image acquisition. Across all similarity metrics, performance decreased slightly compared to the development test set. Similarity metrics were best for data collected with the same knee T/R coil as the training dataset.

Similarity Metric	NMSE (%)		PSNR	CORR	SSIM
avg ± stdev. across patients	*volume*	*cartilage*	*cartilage*	*cartilage*	*volume*
Clinical Data—All	7.35 ± 3.74	4.43 ± 3.61	20.63 ± 2.46	0.84 ± 0.11	0.54 ± 0.08
Clinical—Knee T/R Coil	7.93 ± 3.85	4.17 ± 3.2	20.87 ± 2.37	0.85 ± 0.10	0.57 ± 0.06
Clinical—Flex Coil	4.57 ± 1.28	5.41 ± 4.99	19.89 ± 3.00	0.79 ± 0.17	0.42 ± 0.05
Clinical—Cardiac Coil	7.12 ± 2.96	6.26 ± 3.48	17.93 ± 2.37	0.79 ± 0.10	0.51 ± 0.08
Bilateral Study—Flex Coil	8.93 ± 3.17	7.26 ± 3.55	18.20 ± 2.31	0.76 ± 0.14	0.53 ± 0.06

3.2.3. Quantitative Correlation Analysis

Bland-Altman plots for out-of-distribution data show varied bias, wider limits of agreement (± 4.98 ms or ± 5.1 ms), and weaker correlation compared to in-distribution data, as expected (Figure 6). For data collected in a clinical setting (cohort C), there was minimal negative bias and ground truth $T_{1\rho}$ values averaged 46.38 ± 4.46 ms, similar to the development dataset. For bilateral knee data (cohort D), the ground truth $T_{1\rho}$ values averaged 40.13 ± 3.63 ms and the predicted $T_{1\rho}$ values were on average 5.46 ms higher than the ground truth.
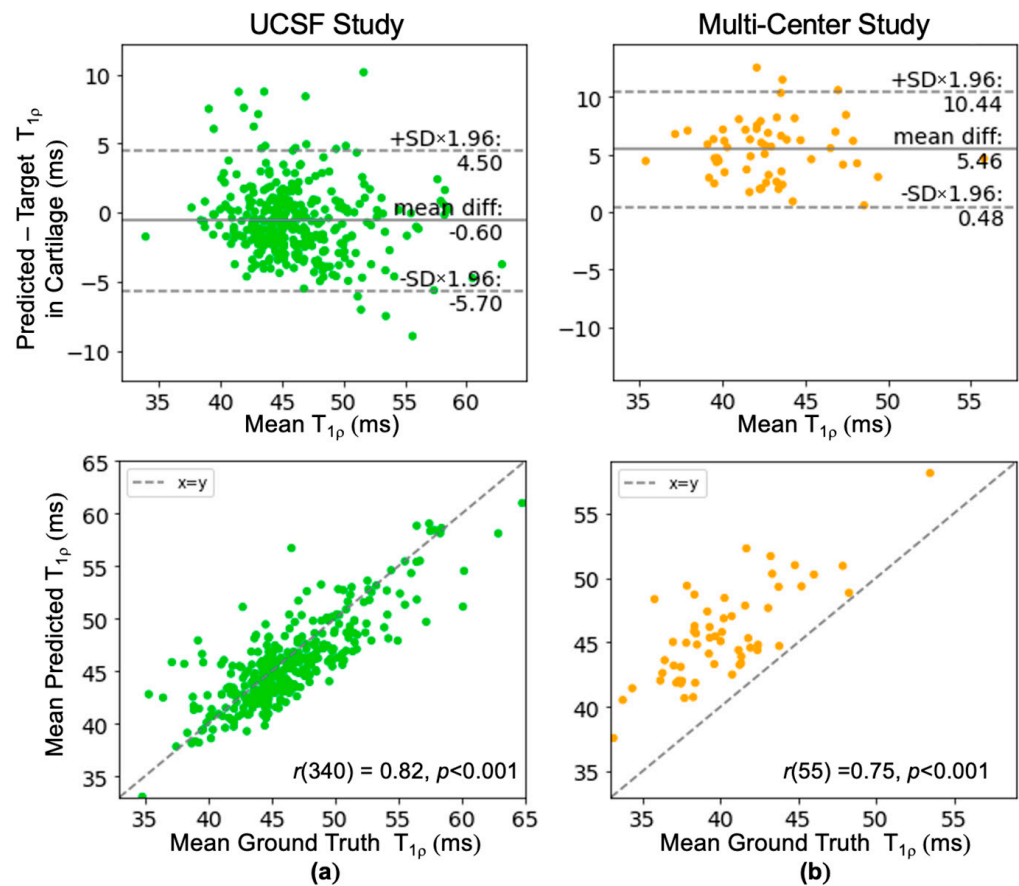

Figure 6. Bland-Altman and correlation plots of out-of-distribution data to evaluate the generalizability of the network. (**a**) Data acquired for the bilateral knee research study at UCSF using two knee coils simultaneously whereas training data was acquired with a unilateral coil. (**b**) Data acquired in a clinical setting had much greater variability in scanners and knee coils used.

Bland-Altman and correlation plots were also created to isolate the effect of the knee T/R, flex, and cardiac coil array on performance (Figure 7). A similar magnitude of bias was observed for the knee T/R coil (-1.13 ms) and flex coil (1.57 ms) while the cardiac coil had the largest bias (4.23 ms). The limits of agreement were slightly higher than training cohort limits for the knee T/R coil ± 4.39 ms, higher for the flex coil ± 5.75 ms, and even higher for the cardiac coil ± 8.92 ms.
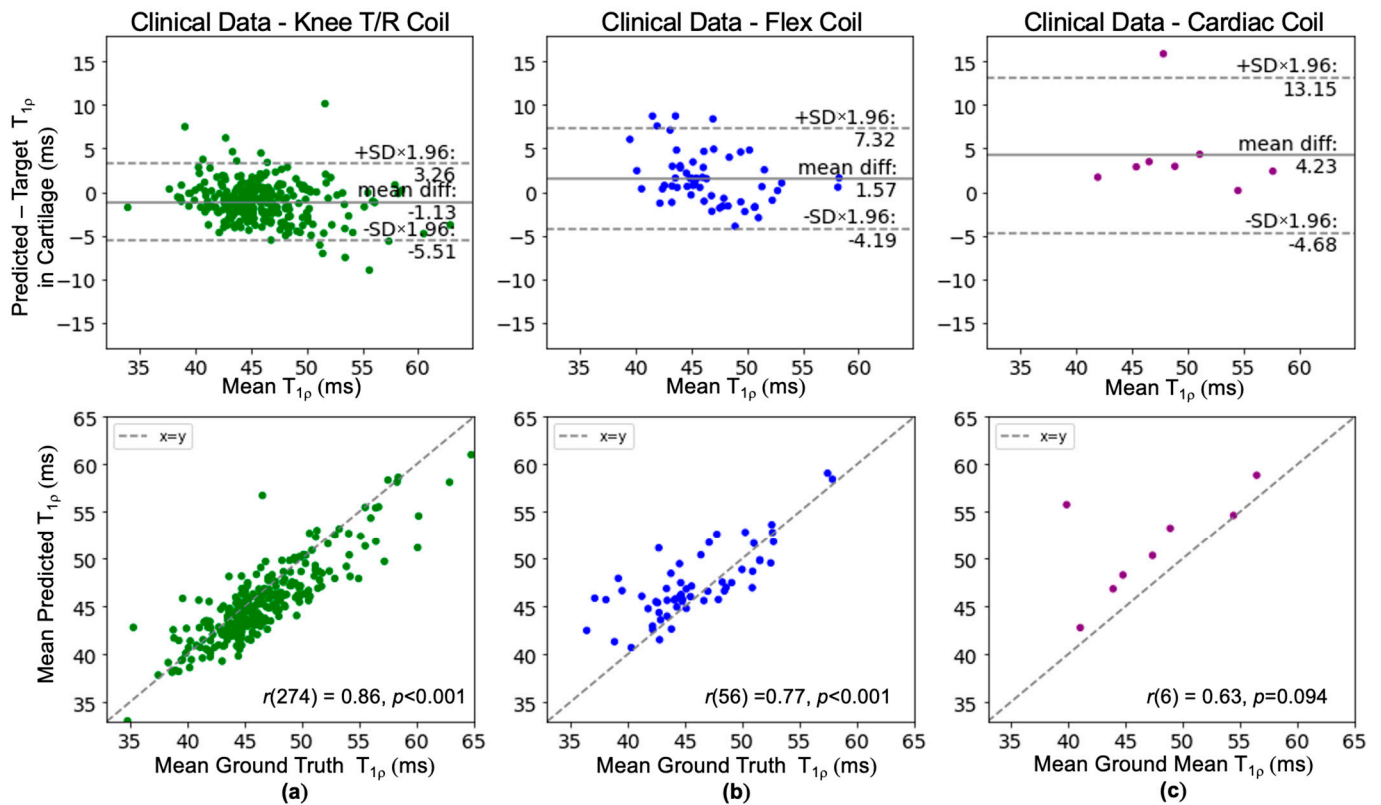
Figure 7. (**a–c**) Bland–Altman and correlation plots for $T_{1\rho}$ images acquired using three different types of knee coils from the clinical dataset (cohort C). Given the knee T/R coil was used in the development dataset, the limits of agreement for the knee T/R coil were narrowest, larger for the flex coil, and widest for the cardiac coil.

4. Discussion

This study presented one of the first networks for quantitative image synthesis in the musculoskeletal domain and conducted comprehensive performance evaluation across four cohorts, two of which had a slight variation in image acquisition settings, scanner, and coil arrays under unforeseen clinical and research settings. Despite these differences, the network generated synthetic T_{1p} maps well, as indicated by low NMSE and similar textures compared to ground truth maps for both healthy and OA knees. This work aimed to explore the performance of the development cohort held-out testing data as well as isolate the network's tolerance to different inputs. Performance was measured in terms of local image intensities and global similarity metrics. Such analysis may capture both the benefits of synthesis as well as challenges with generalizability.

4.1. T_{1p} Synthesis Model Strengths

While there is some degree of correlation between T_2 and T_{1p} relaxation times, prior work has demonstrated the value of utilizing both maps to probe cartilage morphology, particularly at the early stages of disease [23,56]. It has also been shown that T_{1p} is slightly more sensitive to mild OA than T_2 [14]. Consequently, regions of cartilage with variation in texture and elevation patterns are both clinically interesting and challenging areas for synthesis.

Across all cohorts, the network proposed in this study was able to synthesize new information from T_2 maps in areas exhibiting distinct T_{1p} intensity patterns relative to T_2 (Figures 2 and 5). Excellent inference with minimal NMSE in cartilage tissue was observed for in-distribution data while trends in T_{1p} texture and elevation changes relative to T_2 were captured with slightly less accuracy for different scanners and coils. This suggests the network is least sensitive to research and clinical environments but does exhibit some

sensitivity to scan equipment configurations. Proper reconstruction enables texture analysis of T_{1p} profiles that have the potential to detect early or local abnormalities indicative of OA that would otherwise go undetected based on morphological changes [57].

For the held-out test dataset, similarity metric performances indicated exceptional synthesis in relation to several benchmarks for scan/re-scan reproducibility, scan acceleration, and clinical significance. For the same MR system, T_{1p} map cartilage synthesis is limited by in vivo scan/re-scan reproducibility found to be 3.1% (range 1.0–1.7 ms RMS) across 3 sites and 16 knees for cartilage compartments [58]. Cartilage tissue NMSE was within the bounds of variability for re-scanning and the 5.7% quantification error rate was within the limits of clinical significance. Recall that cartilage defects such as lesions or meniscal tears are observed to elevate T_{1p} values within the entire cartilage compartment and surrounding areas [59]. Prior work has identified that 6.4% changes in cartilage T_{1p} [23,24] and 4% to 15% changes in cartilage compartments [27] can be clinically significant for OA diagnosis and management.

Moreover, synthesis performance is comparable to image reconstruction with an acceleration factor of two, as the generated maps are obtained with roughly half the echo images, which is analogous to reducing scan time by half. Reduction in scan time decreases acquisition cost, making clinical adoption of T_{1p} maps more feasible. Prior work has shown that further acceleration of the knee MAPSS sequence by a factor of two introduced 1.49 ms bias and confidence intervals of ± 4.55 ms in the cartilage region [60]. Bland–Altman plots revealed that the network in this study achieved minimal bias (range 0.10–0.45 ms) an order of magnitude lower than similar maps reconstructed with R = 2 acceleration. Although the limits of agreement were wider than the reported range of scan/re-scan variability for fully acquired T_{1p} maps, they were tighter than the limits reported for R = 2 reconstructions of T_2 maps. These results demonstrate the feasibility of synthesis for T_{1p} maps and indicate that synthetic images outperform several reproducibility benchmarks. Additionally, compartment-wide analysis using synthetic images holds clinical value.

For all cohorts, similarity metric performances were highest for cartilage-specific analysis compared to whole image volume assessment likely due to the weighted loss function and noise in the image background. Bias for T_{1p} estimation in these compartments remained minimal while the limits of agreement widened. This may occur due to fewer voxels contributing to the compartment average instead of the entire cartilage region, thereby increasing Bland-Altman sensitivity to variability but not changing the bias. Despite smaller cartilage compartment regions, the network demonstrated robust synthesis since the performance was consistent across mean T_{1p} values for both UCSF (cohort A) and the muti-center study (cohort B) which had a more varied distribution of T_{1p} values in part due to segmentation quality.

4.2. Synthesis Generalizability Assessment on External Datasets

The proposed study has established an initial working baseline for T_{1p} map synthesis. However, widespread usage is limited by the network's ability to generalize to datasets with varied, previously unseen acquisition settings and environments. To investigate network generalizability, synthetic T_{1p} maps were generated from data collected in a clinical setting in addition to standard-of-care imaging and from data collected in a research setting using two flex coils simultaneously for bilateral knee acquisition. The loss function in the proposed network was optimized using both T_{1p} and T_2 map values, which are prone to variance dependent upon acquisition parameters. More specifically, scanner and coil hardware systems may cause slight differences in B0/B1 inhomogeneity patterns that change proton resonance frequencies and excitation profiles. As a result, effects on T_{1p}/T_2 preparations can be different [61,62] such that T_{1p}/T_2 signal decay is affected disproportionately. In addition, multi-coil combination methods for bilateral MRI acquisition were different from others (adaptive coil combination versus standard sum-of-square combination). These reconstruction method variations might also result in a bias for synthetic T1rho maps from bilateral acquisitions. Model performance decreased in both settings but more so in the

bilateral study setting likely due to these differences. Nevertheless, these variations provide valuable insight into the synthesis model.

Data from the clinical setting (cohort C) exhibited similarities to the training dataset with regard to patient population demographics, unilateral knee acquisition, type of scanner used, and type of knee coil used (81% cohort C, n = 278). Differences arose when data were collected using various receive coils: 17% flex coil (n = 57) and 2% cardiac coil to accommodate patient geometries (n = 9). Overall, the network maintained minimal bias (−0.6 ms) for clinical data which was most like the multi-center study bias (−0.45 ms) whose data were primarily acquired on the same scanner.

For clinical data stratified by coil array, network performance was best for data acquired with the same knee T/R coil as the training data, slightly declined for the flex coil, and was the poorest for the cardiac coil. Data acquired with the same coil had bias (−1.13 ms) within the range of scan/re-scan reproducibility. The effect of MR scanner and coil on map values has been quantified by Li et al. in a reproducibility study. The study found in vivo $T_{1\rho}$ and T_2 values for healthy subjects did not have significant differences across sites but did vary depending on the MR system (difference of 2.8 ms for $T_{1\rho}$ and 2.9 ms for T_2 between HDx long bore and MR750 wide bore scanners) and knee coil (difference of 2.8 ms for $T_{1\rho}$ and 4 ms for T_2 between 16PAR flex and QT8PAR knee coils) [38]. For the flex coil data, bias was within the range of scan–re-scan reproducibility. However, for the limited cardiac coil, the bias was greater potentially due to significant observable differences in image SNR and larger patient body shape effect on magnetic field inhomogeneities. Performance changes in limits of agreement and NMSE may be explained by coil differences, such as the use of differing transmit systems (knee coil versus body coil excitation), suggesting future synthesis algorithms may benefit from incorporating scanner information into the network. However, for this network quantification, error rates increased beyond the limit for clinical significance (clinical—all: 11.0%; clinical—knee T/R coil: 9.5%; clinical—flex coil: 12.4%; clinical—cardiac coil: 19.2%) warranting further exploration prior to quantitative evaluation yet qualitative assessment remains feasible.

Primary differences between the bilateral acquisition dataset and training dataset included simultaneous acquisition from two flex coils, updated coil combination software on the scanner, and an older patient population averaging 18 years senior without ACL tear or reconstruction. Prior work by Verschueren et al. found significant increases in T_2 relaxation times with both age and BMI across 109 patients [63], making them covariates of quantitative T_2 mapping for OA detection. While performance was expected to match that of the clinical dataset acquired with the flex coil, performance decreased by +1.85% cartilage NMSE and +3.89 ms bias. At this time, reproducibility metrics involving bilateral acquisition of knee MRI using flex coils are not available. Nevertheless, the differences in the study suggest future work will benefit from a reproducibility study that investigates potential increases in B0/B1 inhomogeneities over two knee volumes and the effects of coil combination software methods. Additionally, age-related differences or usage of two flex coils may have contributed to the overestimation of predicted $T_{1\rho}$ maps. This error can hypothetically be overcome with inference testing of an age-matched population, which was not performed in the proposed study due to the unavailability of such data.

4.3. Network Limitations

In this study, the network performance was constrained by variability in the training dataset, which is consistent with the limitations seen in algorithms trained on local datasets [64]. Despite challenges in obtaining diverse datasets, future endeavors aiming to create clinically useful and broadly applicable networks should prioritize training on datasets containing greater diversity in MR hardware and image reconstruction software. While comparing state-of-the-art algorithms is common practice, this work demonstrates the value of assessing performance on external, inference-only datasets to develop models with greater utility. Additionally, stringent cartilage segmentations were not required

for synthesis evaluation. As a result, this study did not address clinically significant quantitative values although such analyses may be enabled by synthesis in future work.

4.4. Future Direction

Future work may also benefit from the consideration of alternative preprocessing techniques and network architectures that have the potential to be more robust to scanner and coil differences. While 3D V-Nets require additional computational recourses, inputting 3D images as opposed to 2D may allow the network to infer systematic changes in B0/B1 inhomogeneities and the effect of metal artifacts. An end-to-end approach has improved network task performance in other studies and may be explored by synthesizing $T_{1\rho}$ and T_2 maps directly from echo images [65]. Alternatively, model pre-training on a subset of study-specific data or model fine-tuning may improve generalizability across MR scanners, knee coils, patient cohorts, and magnet field strength [66].

Modification to network architectures may include the exploration of variational U-Nets [46,67,68] generative adversarial networks (GANs) [69,70], variational autoencoders [71,72], transformer-based models [73], and other state-of-the-art methods. Additional network modifications may include the incorporation of a contrastive loss term [74] and data augmentation techniques [75]. While this study opted for a data-driven approach to image synthesis, further optimization could be achieved by the incorporation of a contrastive loss term that leverages explicit knowledge of acquisition parameter details (scanner, coil array, repetition times, echo times, etc.) and image SNR. The loss can be integrated into a network discriminator encouraging the generator to produce a scanner-agnostic image, or between the network encoder and decoder, prompting the network to extract features that are agnostic to the scan system.

Prior to widespread adoption, further network development to achieve quantification error rates within the range of clinically relevant changes could provide more confidence in synthetic imaging. Additionally, advancements in standardized coil arrays or calibration could promote greater consistency in $T_{1\rho}$ and T_2 relaxation times, necessary for OA biomarker validation. This need is consistent with findings from a meta-analysis across 55 studies [76]. Such standardization would reduce non-physiological variability thereby presenting a simpler mapping problem for image synthesis.

4.5. Future Application towards Clinical Biomarker Extraction

Alternatively, deep learning algorithms offer high reproducibility and may pose as an alternative for quantitative imaging biomarker standardization and faster clinical translation [77]. Due to the heterogeneity of knee OA, stratification of patient subpopulations based on OA disease onset, stage, and risk of progression is a critical next step to improve early detection and care [78]. By probing tissue cellularity and molecular composition, $T_{1\rho}$ maps have the potential to define diagnostic criteria for OA as well as outcome measures.

However, the Quantitative Imaging Biomarkers Alliance observed limited translation of early-stage knee OA biomarkers into clinical practice due to "variability across devices, sites, patients and time" and are spearheading standardization efforts [30]. Previous studies on MR fingerprinting and quantitative susceptibility mapping have used deep learning algorithms to infer tissue properties from MR signals with the potential for improved accuracy and consistency [44,77,79]. Image synthesis can aid efforts to standardize $T_{1\rho}$ and T_2 measurements of knee cartilage by capturing complex non-linearities between the two sequences to make $T_{1\rho}$ maps accessible. The U-Net proposed in this work, and CNNs in general, create image feature representations highly attuned to the input images. Once a standardized T_2 map is established, quantitative $T_{1\rho}$ biomarkers generated by a CNN can quickly be extracted for data-driven validation and integrated into clinical workflows as a clinical decision-making tool with minimal barriers associated with multi-site data harmonization [78] and clinical translation [80].

5. Conclusions

The network was able to generate synthetic T_{1p} images from T_2 images with excellent fidelity to ground truth T_{1p} images. For data collected across multiple institutions and studies, textures were preserved and the limits of agreement for T_{1p} NMSE were below the limits of clinical relevance. The generalizability of the network showed decreased performance for data acquired in less controlled external datasets, yet variation between MR scanners and coils may account for these differences.

This work shows the capability of deep learning to extract additional diagnostic information from already acquired T_2 maps. With further development, a pipeline like this creates new possibilities for population studies like the OA Initiative, which can add to the characterization of OA, potentially facilitate clinical translation, and complement efforts to establish quantitative imaging biomarkers. Additionally, this study shows the promise of deep learning in accelerating imaging protocols through domain adaptation as opposed to more common reconstruction, standardization, and calibration approaches.

Appendix A

Table A1. Similarity metrics between predicted and ground truth T_{1p} maps for UCSF (cohort A) and multi-center (cohort B) data. Metrics were calculated from the average T_{1p} in entire cartilage region and six cartilage compartments: medial femoral, lateral femoral, medial tibial, lateral tibial, trochlea, and patellar cartilage. Between the entire cartilage region and compartments, performance was quite similar apart from a slight decline in similarity for the multi-center trochlea and patellar cartilage.

| Metric	NMSE (%)		PSNR		CORR	
avg ± stdev.	*UCSF*	*Multi-Center*	*UCSF*	*Multi-Center*	*UCSF*	*Multi-Center*
Cartilage	2.61 ± 1.47	2.18 ± 1.53	24.00 ± 1.78	23.97 ± 2.17	0.85 ± 0.07	0.88 ± 0.08
MF	2.68 ± 1.86	3.08 ± 2.40	22.78 ± 2.35	18.94 ± 2.17	0.82 ± 0.11	0.91 ± 0.07
LF	2.74 ± 1.72	2.86 ± 1.74	23.07 ± 2.16	19.21 ± 2.03	0.84 ± 0.08	0.91 ± 0.05
MT	4.24 ± 3.77	3.02 ± 2.70	22.13 ± 2.96	18.99 ± 2.76	0.82 ± 0.17	0.89 ± 0.07
LT	3.52 ± 3.08	2.71 ± 1.91	23.02 ± 2.49	19.05 ± 2.64	0.87 ± 0.13	0.85 ± 0.19
TROC	2.06 ± 1.03	4.78 ± 2.65	24.18 ± 1.99	16.77 ± 2.31	0.87 ± 0.07	0.81 ± 0.11
PAT	2.04 ± 1.32	5.79 ± 4.39	24.42 ± 2.47	16.83 ± 2.4	0.88 ± 0.06	0.83 ± 0.12
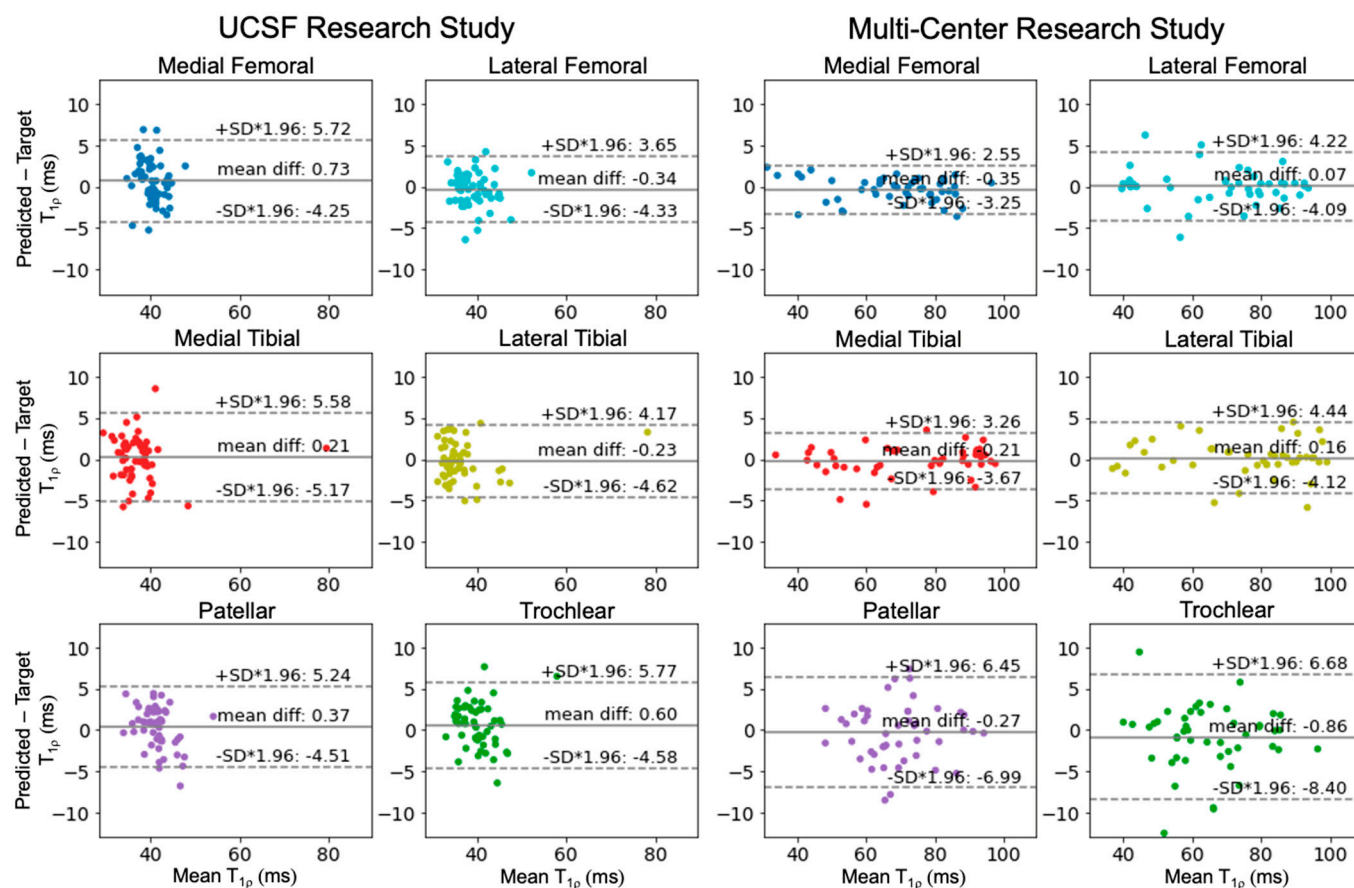
Figure A1. Bland-Altman plots for average $T_{1\rho}$ relaxation times in six cartilage compartments indicated by color across two research studies (cohorts A and B). The solid line shows the bias and the dashed lines show the bias $\pm$ 1.96 times the standard deviation. Bias was minimal ranging from -0.86 to 0.73 ms well within the range of scan/re-scan reproducibility [58]. Limits of agreement were similar across the two studies (range ± 2.90 to ± 5.37 ms) despite varied MR scanner and were similar across compartments, apart from the patellar and trochlear cartilage having slightly wider limits (range ± 4.87 to ± 7.54 ms).

References

1. Wu, A.; March, L.; Zheng, X.; Huang, J.; Wang, X.; Zhao, J.; Blyth, F.M.; Smith, E.; Buchbinder, R.; Hoy, D. Global Low Back Pain Prevalence and Years Lived with Disability from 1990 to 2017: Estimates from the Global Burden of Disease Study 2017. *Ann. Transl. Med.* **2020**, *8*, 299. [CrossRef] [PubMed]
2. Neogi, T. The Epidemiology and Impact of Pain in Osteoarthritis. *Osteoarthr. Cartil.* **2013**, *21*, 1145–1153. [CrossRef] [PubMed]
3. Fox, A.J.S.; Bedi, A.; Rodeo, S.A. The Basic Science of Articular Cartilage: Structure, Composition, and Function. *Sport. Health* **2009**, *1*, 461–468. [CrossRef]
4. Li, X.; Cheng, J.; Lin, K.; Saadat, E.; Bolbos, R.I.; Jobke, B.; Ries, M.D.; Horvai, A.; Link, T.M.; Majumdar, S. Quantitative MRI Using $T_{1\rho}$ and T_2 in Human Osteoarthritic Cartilage Specimens: Correlation with Biochemical Measurements and Histology. *Magn. Reason. Imaging* **2011**, *29*, 324–334. [CrossRef] [PubMed]
5. Hunter, D.J.; Bierma-Zeinstra, S. Osteoarthritis. *Lancet* **2019**, *393*, 1745–1759. [CrossRef]
6. Cui, A.; Li, H.; Wang, D.; Zhong, J.; Chen, Y.; Lu, H. Global, Regional Prevalence, Incidence and Risk Factors of Knee Osteoarthritis in Population-Based Studies. *EClinicalMedicine* **2020**, *29–30*, 100587. [CrossRef] [PubMed]
7. Georgiev, T.; Angelov, A.K. Modifiable Risk Factors in Knee Osteoarthritis: Treatment Implications. *Rheumatol. Int.* **2019**, *39*, 1145–1157. [CrossRef]
8. Arden, N.K.; Perry, T.A.; Bannuru, R.R.; Bruyère, O.; Cooper, C.; Haugen, I.K.; Hochberg, M.C.; McAlindon, T.E.; Mobasheri, A.; Reginster, J.-Y. Non-Surgical Management of Knee Osteoarthritis: Comparison of ESCEO and OARSI 2019 Guidelines. *Nat. Rev. Rheumatol.* **2021**, *17*, 59–66. [CrossRef]
9. Billesberger, L.M.; Fisher, K.M.; Qadri, Y.J.; Boortz-Marx, R.L. Procedural Treatments for Knee Osteoarthritis: A Review of Current Injectable Therapies. *Pain Res. Manag.* **2020**, *2020*, 3873098. [CrossRef]

10. Gress, K.; Charipova, K.; An, D.; Hasoon, J.; Kaye, A.D.; Paladini, A.; Varrassi, G.; Viswanath, O.; Abd-Elsayed, A.; Urits, I. Treatment Recommendations for Chronic Knee Osteoarthritis. *Best Pract. Res. Clin. Anaesthesiol.* **2020**, *34*, 369–382. [CrossRef]

11. Altman, R.; Asch, E.; Bloch, D.; Bole, G.; Borenstein, D.; Brandt, K.; Christy, W.; Cooke, T.D.; Greenwald, R.; Hochberg, M.; et al. Development of Criteria for the Classification and Reporting of Osteoarthritis: Classification of Osteoarthritis of the Knee. *Arthritis Rheum.* **1986**, *29*, 1039–1049. [CrossRef] [PubMed]

12. Katz, J.N.; Arant, K.R.; Loeser, R.F. Diagnosis and Treatment of Hip and Knee Osteoarthritis. *JAMA* **2021**, *325*, 568. [CrossRef] [PubMed]

13. Peat, G.; Thomas, E.; Duncan, R.; Wood, L.; Hay, E.; Croft, P. Clinical Classification Criteria for Knee Osteoarthritis: Performance in the General Population and Primary Care. *Ann. Rheum. Dis.* **2006**, *65*, 1363–1367. [CrossRef] [PubMed]

14. Hunter, D.J.; Felson, D.T. Osteoarthritis. *BMJ* **2006**, *332*, 639–642. [CrossRef] [PubMed]

15. Ding, C.; Cicuttini, F.; Jones, G. How Important Is MRI for Detecting Early Osteoarthritis? *Nat. Clin. Pract. Rheumatol.* **2008**, *4*, 4–5. [CrossRef] [PubMed]

16. Roemer, F.W.; Kwoh, C.K.; Hayashi, D.; Felson, D.T.; Guermazi, A. The Role of Radiography and MRI for Eligibility Assessment in DMOAD Trials of Knee OA. *Nat. Rev. Rheumatol.* **2018**, *14*, 372–380. [CrossRef] [PubMed]

17. Mathiessen, A.; Cimmino, M.A.; Hammer, H.B.; Haugen, I.K.; Iagnocco, A.; Conaghan, P.G. Imaging of Osteoarthritis (OA): What Is New? *Best Pract. Res. Clin. Rheumatol.* **2016**, *30*, 653–669. [CrossRef]

18. Hayashi, D.; Roemer, F.W.; Guermazi, A. Imaging of Osteoarthritis by Conventional Radiography, MR Imaging, PET–Computed Tomography, and PET–MR Imaging. *PET Clin.* **2019**, *14*, 17–29. [CrossRef]

19. Krakowski, P.; Karpiński, R.; Jojczuk, M.; Nogalska, A.; Jonak, J. Knee MRI Underestimates the Grade of Cartilage Lesions. *Appl. Sci.* **2021**, *11*, 1552. [CrossRef]

20. Roemer, F.W.; Engelke, K.; Li, L.; Laredo, J.-D.; Guermazi, A. MRI Underestimates Presence and Size of Knee Osteophytes Using CT as a Reference Standard. *Osteoarthr. Cartil.* **2023**, *31*, 656–668. [CrossRef]

21. Marinetti, A.; Tessarolo, F.; Ventura, L.; Falzone, A.; Neri, M.; Piccoli, F.; Rigoni, M.; Masè, M.; Cortese, F.; Nollo, G.; et al. Morphological MRI of Knee Cartilage: Repeatability and Reproducibility of Damage Evaluation and Correlation with Gross Pathology Examination. *Eur. Radiol.* **2020**, *30*, 3226–3235. [CrossRef] [PubMed]

22. Li, X.; Benjamin Ma, C.; Link, T.M.; Castillo, D.-D.; Blumenkrantz, G.; Lozano, J.; Carballido-Gamio, J.; Ries, M.; Majumdar, S. In Vivo T1ρ and T2 Mapping of Articular Cartilage in Osteoarthritis of the Knee Using 3T MRI. *Osteoarthr. Cartil.* **2007**, *15*, 789–797. [CrossRef] [PubMed]

23. Stahl, R.; Luke, A.; Li, X.; Carballido-Gamio, J.; Ma, C.B.; Majumdar, S.; Link, T.M. T1rho, T2 and Focal Knee Cartilage Abnormalities in Physically Active and Sedentary Healthy Subjects versus Early OA Patients—A 3.0-Tesla MRI Study. *Eur. Radiol.* **2009**, *19*, 132–143. [CrossRef] [PubMed]

24. Li, X.; Kuo, D.; Theologis, A.; Carballido-Gamio, J.; Stehling, C.; Link, T.M.; Ma, C.B.; Majumdar, S. Cartilage in Anterior Cruciate Ligament–Reconstructed Knees: MR Imaging T1$_\rho$ and T2—Initial Experience with 1-Year Follow-Up. *Radiology* **2011**, *258*, 505–514. [CrossRef] [PubMed]

25. MacKay, J.W.; Low, S.B.L.; Smith, T.O.; Toms, A.P.; McCaskie, A.W.; Gilbert, F.J. Systematic Review and Meta-Analysis of the Reliability and Discriminative Validity of Cartilage Compositional MRI in Knee Osteoarthritis. *Osteoarthr. Cartil.* **2018**, *26*, 1140–1152. [CrossRef] [PubMed]

26. Le, J.; Peng, Q.; Sperling, K. Biochemical Magnetic Resonance Imaging of Knee Articular Cartilage: T1rho and T2 Mapping as Cartilage Degeneration Biomarkers. *Ann. N. Y. Acad. Sci.* **2016**, *1383*, 34–42. [CrossRef] [PubMed]

27. Pietrosimone, B.; Nissman, D.; Padua, D.A.; Blackburn, J.T.; Harkey, M.S.; Creighton, R.A.; Kamath, G.M.; Healy, K.; Schmitz, R.; Driban, J.B.; et al. Associations between Cartilage Proteoglycan Density and Patient Outcomes 12 Months Following Anterior Cruciate Ligament Reconstruction. *Knee* **2018**, *25*, 118–129. [CrossRef]

28. Mlynárik, V.; Trattnig, S.; Huber, M.; Zembsch, A.; Imhof, H. The Role of Relaxation Times in Monitoring Proteoglycan Depletion in Articular Cartilage. *J. Magn. Reason. Imaging* **1999**, *10*, 497–502. [CrossRef]

29. Soellner, S.T.; Goldmann, A.; Muelheims, D.; Welsch, G.H.; Pachowsky, M.L. Intraoperative Validation of Quantitative T2 Mapping in Patients with Articular Cartilage Lesions of the Knee. *Osteoarthr. Cartil.* **2017**, *25*, 1841–1849. [CrossRef]

30. Chalian, M.; Li, X.; Guermazi, A.; Obuchowski, N.A.; Carrino, J.A.; Oei, E.H.; Link, T.M.; Boss, M.; Botto-van Bemden, A.; Boutin, R.; et al. The QIBA Profile for MRI-Based Compositional Imaging of Knee Cartilage. *Radiology* **2021**, *301*, 423–432. [CrossRef]

31. Obuchowski, N.A.; Reeves, A.P.; Huang, E.P.; Wang, X.-F.; Buckler, A.J.; Kim, H.J.; Barnhart, H.X.; Jackson, E.F.; Giger, M.L.; Pennello, G.; et al. Quantitative Imaging Biomarkers: A Review of Statistical Methods for Computer Algorithm Comparisons. *Stat. Methods Med. Res.* **2015**, *24*, 68–106. [CrossRef] [PubMed]

32. Link, T.M.; Joseph, G.B.; Li, X. MRI-Based T$_{1rho}$ and T$_2$ Cartilage Compositional Imaging in Osteoarthritis: What Have We Learned and What Is Needed to Apply It Clinically and in a Trial Setting? *Skelet. Radiol.* **2023**, *52*, 2137–2147. [CrossRef] [PubMed]

33. Han, M.; Tibrewala, R.; Bahroos, E.; Pedoia, V.; Majumdar, S. Magnetization-prepared Spoiled Gradient-echo Snapshot Imaging for Efficient Measurement of R2-R1ρ in Knee Cartilage. *Magn. Reason. Med.* **2022**, *87*, 733–745. [CrossRef] [PubMed]

34. Pedoia, V.; Haefeli, J.; Morioka, K.; Teng, H.; Nardo, L.; Souza, R.B.; Ferguson, A.R.; Majumdar, S. MRI and Biomechanics Multidimensional Data Analysis Reveals R2-R1ρ as an Early Predictor of Cartilage Lesion Progression in Knee Osteoarthritis. *J. Magn. Reson. Imaging* **2018**, *47*, 78–90. [CrossRef] [PubMed]

35. Russell, C.; Pedoia, V.; Majumdar, S. Composite Metric R2 − R1ρ (1/T2 − 1/T1ρ) as a Potential MR Imaging Biomarker Associated with Changes in Pain after ACL Reconstruction: A Six-month Follow-up. *J. Orthop. Res.* **2017**, *35*, 718–729. [CrossRef] [PubMed]

36. Nevitt, M.; Felson, D.; Lester, G. The Osteoarthritis Initiative. *Protoc. Cohort Study* **2006**, *1*, 1–155.

37. Wang, T.; Lei, Y.; Fu, Y.; Wynne, J.F.; Curran, W.J.; Liu, T.; Yang, X. A Review on Medical Imaging Synthesis Using Deep Learning and Its Clinical Applications. *J. Appl. Clin. Med. Phys.* **2021**, *22*, 11–36. [CrossRef]

38. Sorin, V.; Barash, Y.; Konen, E.; Klang, E. Creating Artificial Images for Radiology Applications Using Generative Adversarial Networks (GANs)—A Systematic Review. *Acad. Radiol.* **2020**, *27*, 1175–1185. [CrossRef]

39. Fayad, L.M.; Parekh, V.S.; de Castro Luna, R.; Ko, C.C.; Tank, D.; Fritz, J.; Ahlawat, S.; Jacobs, M.A. A Deep Learning System for Synthetic Knee Magnetic Resonance Imaging. *Investig. Radiol.* **2021**, *56*, 357–368. [CrossRef]

40. Gan, H.-S.; Ramlee, M.H.; Al-Rimy, B.A.S.; Lee, Y.-S.; Akkaraekthalin, P. Hierarchical Knee Image Synthesis Framework for Generative Adversarial Network: Data From the Osteoarthritis Initiative. *IEEE Access* **2022**, *10*, 55051–55061. [CrossRef]

41. Jaouen, V.; Dardenne, G.; Tixier, F.; Stindel, E.; Visvikis, D. Effect of GAN-Based Image Standardization on MR Knee Bone Tissue Classification Performance. In Proceedings of the CAOS 2020: 20th Annual Meeting of the International Society for Computer Assisted Orthopedic Surgery, Brest, France, 10–13 June 2020; pp. 126–130.

42. Kaji, S.; Kida, S. Overview of Image-to-Image Translation by Use of Deep Neural Networks: Denoising, Super-Resolution, Modality Conversion, and Reconstruction in Medical Imaging. *Radiol. Phys. Technol.* **2019**, *12*, 235–248. [CrossRef] [PubMed]

43. Salehi, A.W.; Khan, S.; Gupta, G.; Alabduallah, B.I.; Almjally, A.; Alsolai, H.; Siddiqui, T.; Mellit, A. A Study of CNN and Transfer Learning in Medical Imaging: Advantages, Challenges, Future Scope. *Sustainability* **2023**, *15*, 5930. [CrossRef]

44. Fritz, B.; Fritz, J. Artificial Intelligence for MRI Diagnosis of Joints: A Scoping Review of the Current State-of-the-Art of Deep Learning-Based Approaches. *Skelet. Radiol.* **2022**, *51*, 315–329. [CrossRef] [PubMed]

45. Siddique, N.; Paheding, S.; Elkin, C.P.; Devabhaktuni, V. U-Net and Its Variants for Medical Image Segmentation: A Review of Theory and Applications. *IEEE Access* **2021**, *9*, 82031–82057. [CrossRef]

46. Azad, R.; Aghdam, E.K.; Rauland, A.; Jia, Y.; Avval, A.H.; Bozorgpour, A.; Karimijafarbigloo, S.; Cohen, J.P.; Adeli, E.; Merhof, D. Medical Image Segmentation Review: The Success of U-Net. *arXiv* **2022**, arXiv:2211.14830.

47. Su, F.; Pedoia, V.; Teng, H.-L.; Kretzschmar, M.; Lau, B.C.; McCulloch, C.E.; Link, T.M.; Ma, C.B.; Li, X. The Association between MR T1ρ and T2 of Cartilage and Patient-Reported Outcomes after ACL Injury and Reconstruction. *Osteoarthr. Cartil.* **2016**, *24*, 1180–1189. [CrossRef] [PubMed]

48. Pedoia, V.; Russell, C.; Randolph, A.; Li, X.; Majumdar, S.; Consortium, A.-A. Principal Component Analysis-T1ρ Voxel Based Relaxometry of the Articular Cartilage: A Comparison of Biochemical Patterns in Osteoarthritis and Anterior Cruciate Ligament Subjects. *Quant. Imaging Med. Surg.* **2016**, *6*, 623–633. [CrossRef]

49. Li, X.; Han, E.T.; Busse, R.F.; Majumdar, S. In Vivo T1ρ Mapping in Cartilage Using 3D Magnetization-prepared Angle-modulated Partitioned K-space Spoiled Gradient Echo Snapshots (3D MAPSS). *Magn. Reason. Med.* **2008**, *59*, 298–307. [CrossRef]

50. Pluim, J.P.W.; Maintz, J.B.A.; Viergever, M.A. Mutual-Information-Based Registration of Medical Images: A Survey. *IEEE Trans. Med. Imaging* **2003**, *22*, 986–1004. [CrossRef]

51. Moré, J.J. The Levenberg-Marquardt Algorithm: Implementation and Theory. In *Numerical Analysis: Proceedings of the Biennial Conference Held at Dundee, 28 June–1 July 1977*; Springer: Berlin, Heidelberg, 1978; pp. 105–116.

52. Astuto, B.; Flament, I.K.; Namiri, N.; Shah, R.; Bharadwaj, U.M.; Link, T.D.; Bucknor, M.; Pedoia, V.; Majumdar, S. Automatic Deep Learning–Assisted Detection and Grading of Abnormalities in Knee MRI Studies. *Radiol. Artif. Intell.* **2021**, *3*, e200165. [CrossRef]

53. Kremelberg, D. *Practical Statistics: A Quick and Easy Guide to IBM® SPSS® Statistics, STATA, and Other Statistical Software*; SAGE Publications, Inc.: Thousand Oaks, CA, USA, 2011; ISBN 9781412974943.

54. Giavarina, D. Understanding Bland Altman Analysis. *Biochem. Med.* **2015**, *25*, 141–151. [CrossRef] [PubMed]

55. Gerke, O. Reporting Standards for a Bland–Altman Agreement Analysis: A Review of Methodological Reviews. *Diagnostics* **2020**, *10*, 334. [CrossRef] [PubMed]

56. Yang, Z.; Xie, C.; Ou, S.; Zhao, M.; Lin, Z. Cutoff Points of T1 Rho/T2 Mapping Relaxation Times Distinguishing Early-Stage and Advanced Osteoarthritis. *Arch. Med. Sci.* **2022**, *18*, 1004. [CrossRef] [PubMed]

57. Nozaki, T.; Kaneko, Y.; Yu, H.J.; Kaneshiro, K.; Schwarzkopf, R.; Hara, T.; Yoshioka, H. T1rho Mapping of Entire Femoral Cartilage Using Depth- and Angle-Dependent Analysis. *Eur. Radiol.* **2016**, *26*, 1952–1962. [CrossRef] [PubMed]

58. Li, X.; Pedoia, V.; Kumar, D.; Rivoire, J.; Wyatt, C.; Lansdown, D.; Amano, K.; Okazaki, N.; Savic, D.; Koff, M.F.; et al. Cartilage T1ρ and T2 Relaxation Times: Longitudinal Reproducibility and Variations Using Different Coils, MR Systems and Sites. *Osteoarthr. Cartil.* **2015**, *23*, 2214–2223. [CrossRef] [PubMed]

59. Souza, R.B.; Feeley, B.T.; Zarins, Z.A.; Link, T.M.; Li, X.; Majumdar, S. T1rho MRI Relaxation in Knee OA Subjects with Varying Sizes of Cartilage Lesions. *Knee* **2013**, *20*, 113–119. [CrossRef]

60. Tolpadi, A.A.; Han, M.; Calivà, F.; Pedoia, V.; Majumdar, S. Region of Interest-Specific Loss Functions Improve T2 Quantification with Ultrafast T2 Mapping MRI Sequences in Knee, Hip and Lumbar Spine. *Sci. Rep.* **2022**, *12*, 22208. [CrossRef]

61. Chen, W.; Takahashi, A.; Han, E. Quantitative T1ρ Imaging Using Phase Cycling for B0 and B1 Field Inhomogeneity Compensation. *Magn. Reason. Imaging* **2011**, *29*, 608–619. [CrossRef]

62. Foltz, W.D.; Stainsby, J.A.; Wright, G.A. T2 Accuracy on a Whole-Body Imager. *Magn. Reason. Med.* **1997**, *38*, 759–768. [CrossRef]

63. Verschueren, J.; Van Langeveld, S.J.; Dragoo, J.L.; Bierma-Zeinstra, S.M.A.; Reijman, M.; Gold, G.E.; Oei, E.H.G. T2 Relaxation Times of Knee Cartilage in 109 Patients with Knee Pain and Its Association with Disease Characteristics. *Acta Orthop.* **2021**, *92*, 335–340. [CrossRef]

64. Punn, N.S.; Agarwal, S. Modality Specific U-Net Variants for Biomedical Image Segmentation: A Survey. *Artif. Intell. Rev.* **2022**, *55*, 5845–5889. [CrossRef] [PubMed]

65. Tolpadi, A.A.; Bharadwaj, U.; Gao, K.T.; Bhattacharjee, R.; Gassert, F.G.; Luitjens, J.; Giesler, P.; Morshuis, J.N.; Fischer, P.; Hein, M.; et al. K2S Challenge: From Undersampled K-Space to Automatic Segmentation. *Bioengineering* **2023**, *10*, 267. [CrossRef] [PubMed]

66. Moya-Sáez, E.; Peña-Nogales, Ó.; de Luis-García, R.; Alberola-López, C. A Deep Learning Approach for Synthetic MRI Based on Two Routine Sequences and Training with Synthetic Data. *Comput. Methods Programs Biomed.* **2021**, *210*, 106371. [CrossRef] [PubMed]

67. Jia, X.; Bartlett, J.; Zhang, T.; Lu, W.; Qiu, Z.; Duan, J. U-Net vs Transformer: Is U-Net Outdated in Medical Image Registration? In Proceedings of the International Workshop on Machine Learning in Medical Imaging, Singapore, 18 September 2022; Springer Nature: Cham, Switzerland, 2022; pp. 151–160.

68. Salpea, N.; Tzouveli, P.; Kollias, D. Medical Image Segmentation: A Review of Modern Architectures. In Proceedings of the European Conference on Computer Vision, Paris, France, 2–6 October 2023; Springer Nature: Cham, Switzerland, 2023; pp. 691–708.

69. Pan, K.; Cheng, P.; Huang, Z.; Lin, L.; Tang, X. Transformer-Based T2-Weighted MRI Synthesis from T1-Weighted Images. In Proceedings of the 2022 44th Annual International Conference of the IEEE Engineering in Medicine & Biology Society (EMBC), Glasgow, UK, 11–15 July 2022; IEEE: New York, NY, USA, 2022; pp. 5062–5065.

70. Zhu, J.-Y.; Park, T.; Isola, P.; Efros, A.A. Unpaired Image-to-Image Translation Using Cycle-Consistent Adversarial Networks. In Proceedings of the IEEE International Conference on Computer Vision, Venice, Italy, 22–29 October 2017; pp. 2223–2232.

71. Huang, H.; Li, Z.; He, R.; Sun, Z.; Tan, T. IntroVAE: Introspective Variational Autoencoders for Photographic Image Synthesis. *Adv. Neural Inf. Process. Syst.* **2018**, *31*. [CrossRef]

72. Cao, B.; Bi, Z.; Hu, Q.; Zhang, H.; Wang, N.; Gao, X.; Shen, D. AutoEncoder-Driven Multimodal Collaborative Learning for Medical Image Synthesis. *Int. J. Comput. Vis.* **2023**, *131*, 1995–2014. [CrossRef]

73. Liu, J.; Pasumarthi, S.; Duffy, B.; Gong, E.; Datta, K.; Zaharchuk, G. One Model to Synthesize Them All: Multi-Contrast Multi-Scale Transformer for Missing Data Imputation. *IEEE Trans. Med. Imaging* **2023**, *42*, 2577–2591. [CrossRef] [PubMed]

74. Touati, R.; Kadoury, S. Bidirectional Feature Matching Based on Deep Pairwise Contrastive Learning for Multiparametric MRI Image Synthesis. *Phys. Med. Biol.* **2023**, *68*, 125010. [CrossRef]

75. Chlap, P.; Min, H.; Vandenberg, N.; Dowling, J.; Holloway, L.; Haworth, A. A Review of Medical Image Data Augmentation Techniques for Deep Learning Applications. *J. Med. Imaging Radiat. Oncol.* **2021**, *65*, 545–563. [CrossRef]

76. Atkinson, H.F.; Birmingham, T.B.; Moyer, R.F.; Yacoub, D.; Kanko, L.E.; Bryant, D.M.; Thiessen, J.D.; Thompson, R.T. MRI T2 and T1ρ Relaxation in Patients at Risk for Knee Osteoarthritis: A Systematic Review and Meta-Analysis. *BMC Musculoskelet. Disord.* **2019**, *20*, 182. [CrossRef]

77. European Society of Radiology (ESR). Magnetic Resonance Fingerprinting—A Promising New Approach to Obtain Standardized Imaging Biomarkers from MRI. *Insights Imaging* **2015**, *6*, 163–165. [CrossRef]

78. Mahmoudian, A.; Lohmander, L.S.; Mobasheri, A.; Englund, M.; Luyten, F.P. Early-Stage Symptomatic Osteoarthritis of the Knee—Time for Action. *Nat. Rev. Rheumatol.* **2021**, *17*, 621–632. [CrossRef] [PubMed]

79. Lundervold, A.S.; Lundervold, A. An Overview of Deep Learning in Medical Imaging Focusing on MRI. *Z Med. Phys.* **2019**, *29*, 102–127. [CrossRef] [PubMed]

80. Kraus, V.B.; Karsdal, M.A. Osteoarthritis: Current Molecular Biomarkers and the Way Forward. *Calcif. Tissue Int.* **2021**, *109*, 329–338. [CrossRef] [PubMed]